Research in Astronomy and Astrophysics, 24:045005 (11pp), 2024 April https://doi.org/10.1088/1674-4527/ad24f6

Development of a Front End Array for Broadband Phased Array Receiver

Kai Wang[1,2,3], Liang Cao[1,3], Jun Ma[1,3], Xue-Feng Duan[1,3], Hao Yan[1,3], Mao-Zheng Chen[1,3], and Yun-Wei Ning[1,3]
[1] Xinjiang Astronomical Observatory, Chinese Academy of Sciences, Urumqi 830011, China; wangkai@xao.ac.cn, chen@xao.ac.cn
[2] University of the Chinese Academy of Sciences, Beijing 100049, China
[3] Xinjiang Key Laboratory of Microwave Technology, Urumqi 830011, China
Received 2023 October 11; revised 2024 January 25; accepted 2024 January 29; published 2024 March 26

Abstract

The receiver is a signal receiving device placed at the focus of the telescope. In order to improve the observation efficiency, the concept of phased array receiver has been proposed in recent years, which places a small phased array at the focal plane of the reflector, and flexible pattern and beam scanning functions can be achieved through a beamforming network. If combined with the element multiplexing, all beams within the entire field of view can be observed simultaneously to achieve continuous sky coverage. This article focuses on the front-end array of phased array receiver at 0.7–1.8 GHz for QiTai Telescope, and designs a Vivaldi antenna array of PCB structure with dual line polarization. Each polarization antenna is designed to arrange in a rectangle manner by 11 × 10. Based on the simulation results of the focal field, 32, 18, and eight elements were selected to form one beam at 0.7, 1.25, and 1.8 GHz. An analog beamforming network was constructed, and the measured gains of axial beam under uniform weighting were 19.32, 13.72, and 15.22 dBi. Combining the beam scanning method of reflector antenna, the pattern test of different position element sets required for PAF beam scanning was carried out under independent array. The pattern optimization at 1.25 GHz was carried out by weighting method of conjugate field matching. Compared with uniform weighting, the gain, sidelobe level, and main beam direction under conjugate field matching have been improved. Although the above test and simulation results are slightly different, which is related to the passive array and laboratory testing condition, the relevant work has accumulated experience in the development of the front-end array for the phased array receiver, and has good guiding significance for future performance verification after the array is installed on the telescope.

Key words: telescopes – instrumentation: detectors – techniques: radar astronomy

1. Introduction

A phased array receiver is a cutting-edge signal receiving technology in the field of radio astronomy in recent years. This technology arranges several electric small antenna units in a certain way at the focal plane of a radio telescope, and applies excitation to each array element through a beamforming network to adjust the amplitude and phase of each array element. Combined with the array element multiplexing function, multiple overlapping beams are formed instantaneously, achieving continuous field of view coverage and improving the efficiency of radio telescope sky survey (Wu 2013). Compared to traditional multi beam receiver, the front-end of a phased array receiver is more similar to a traditional phased array antenna. However, due to its placement in the focal plane of a radio telescope to replace the traditional feed, it is also called as Phased Array Feed (PAF) in the field of radio astronomy (Wu et al. 2013).

Many relevant research institutions internationally have conducted extensive theoretical research and engineering practice on PAF receiver. Currently, the main applications of PAF receiver to single aperture large radio telescopes include FLAG (Focal *L* band Array for GBT) assembled for GBT (Roshi et al. 2018) and AO19 cryo-PAF assembled for the former Arecibo telescope (Cortes-Medellin et al. 2015) in the United States, and the installation, debugging, and trial observation of the modified Mark II PAF were carried out on Parks in Australia (Chippendale et al. 2016) and Effelsberg in Germany (Deng et al. 2017), as shown in Figure 1.

The construction of the QiTai 110 m aperture radio telescope project of Xinjiang Astronomical Observatory (XAO), Chinese Academy of Sciences has started (Wang 2014), in which the planned 20 cm band (0.7–1.8 GHz) PAF is the only phased array receiver (Wang et al. 2023), and related technology research and development has been carried out. This article combines the technical requirements of the 20 cm band PAF receiver to design the front-end feed array, fabricate the prototype of antenna array, and conduct actual measurement and verification based on the conditions of the microwave technology laboratory of XAO.

2. Array Design of PAF Receiver

2.1. Analysis of Focal Field

Due to the front-end array of PAF is placed on the focal plane of the reflector, in addition to considering the working

Figure 1. Mark II PAF receiver installed on Parks 64 m telescope.

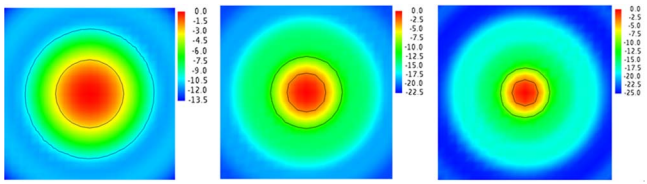

Figure 2. Simulation results of focal field at 0.7, 1.25 and 1.8 GHz.

frequency, it is also necessary to consider the parameters of the reflector, such as the focal diameter ratio and aperture, when designing the array. Considering that the energy distribution of the focal field is independent of the antenna aperture (He & Li 2013), and simulating the focal field of a 110 m aperture reflector will take a lot of time, in order to quickly and efficiently conduct focal field analysis, we use a 4 m aperture reflector with a focal diameter ratio of 0.33, which is consistent with the QiTai Telescope, for relevant simulation and design.

First, set the focal field size to 0.6 m × 0.6 m, combined with the operating frequency of 0.7–1.8 GHz for the 20 cm band PAF, three typical frequency points of 0.7, 1.25 and 1.8 GHz were selected for focal field simulation. The simulation results of the normalized focal field at the three frequency points are shown in Figure 2.

The circular areas shown by the black lines in Figure 2 are the −3 and −10 dB edge taper areas after the normalization of the electric field at three frequency points. It can be seen that as the wavelength shortens, the edge taper area of the focal plane field also decreases. From reference (Tian 2023), it can be concluded that at a focal diameter ratio of 0.33, the energy captured by the −10 dB edge taper area is within 70%. If we want to receive more energy, the PAF array needs to be arranged beyond this area. For example, it can cover a larger area of the first or third zero depth (Tian et al. 2022), but this will simultaneously increase the size and number of the array, affect the overall weight, cost, and cooling design of the receiver, and also put higher requirements on the data processing ability of the digital terminal. Therefore, when designing PAF array, the setting of array size still needs to be balanced.

2.2. Design of Array

In the basic design indicators of the array for 20 cm band PAF (Ma et al. 2019), in addition to the number of array elements in the order of 100, the array also needs to achieve a working bandwidth of 0.7–1.8 GHz, especially for the design of a 2.5 octave broadband array, the selection and layout of array elements are crucial.

2.2.1. Selection of Array Elements

There are many types of antennas, and the antenna elements used in a PAF array mainly include microstrip antennas (Hay et al. 2007), octagonal ring antennas (Zhang & Brown 2011), dipole antennas (Roshi et al. 2018), and Vivaldi antennas (Navarrini et al. 2018). At present, Australia has developed a fully cooled PAF array for the Parkes 64 m radio telescope, the array element is a rocket type antenna, which is an optimized metal Vivaldi antenna that can achieve a working bandwidth of 0.7–1.98 GHz when applied to the array (Dunning 2022). Considering the operating bandwidth of the existing antennas and the requirement of 0.7–1.8 GHz, we select the Vivaldi antenna with the most potential to achieve broadband characteristics as the array element.

The Vivaldi antenna is a broadband slot antenna proposed by Gibson in 1979 that gradually changes exponentially. It couples energy onto the antenna patch through microstrip transmission lines and radiates it out. When the Vivaldi antenna was located in the array, the antenna array instead exhibited ultra wideband performance. After theoretical analysis, the working principle of this ultra wideband antenna array is similar to that of Munk's strongly coupled dipole array, further demonstrating the correctness of the broadband Vivaldi antenna array theory based on enhanced coupling.

2.2.2. Layout of Array

Based on the above Vivaldi antenna selection and tightly coupled antenna array arrangement design, combined with the dual line polarization requirements, Vivaldi antenna array is arranged in a rectangular manner. The elements are made of PCB material Vivaldi antennas, and the same polarized antennas are arranged in a 10 × 11 manner.

This article defines the two linear polarization of the array as horizontal and vertical polarization. After multiple iterations to optimize the design parameters of the Vivaldi antenna, the simulation results of the return loss of the two polarized central elements under uniform excitation of the entire array are shown in Figure 3. It can be seen that the return loss has basically

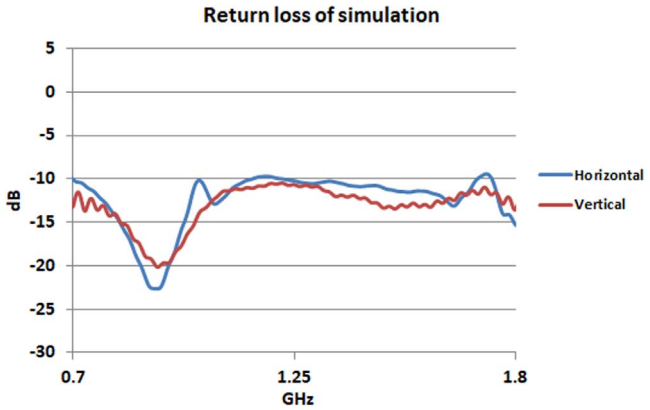

Figure 3. Simulation results of return loss for horizontal and vertical polarized central elements.

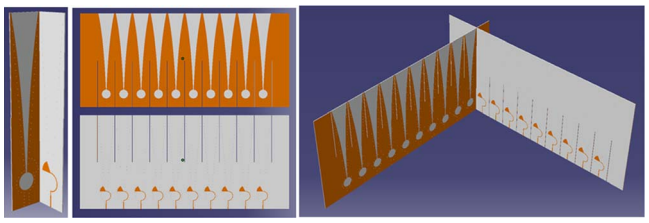

Figure 4. Vivaldi antenna and array assembly model.

reached below −10 dB within the operating bandwidth of 0.7–1.8 GHz. From the simulation results of the return loss, it can be seen that this Vivaldi antenna array meets the bandwidth requirement of 0.7–1.8 GHz.

The Vivaldi antenna array selects a PCB with a dielectric constant of 3.85 and a thickness of 0.8 mm. The independent Vivaldi antenna has a width of 30.025 mm and a height of 161 mm. The antenna model is shown in Figure 4. In order to facilitate the overall processing and assembly of the array, a rectangular array is formed by cross installation of two linear polarized antenna array. The single row antenna array with the opening slot above is set as horizontal polarization, and the cross installation of the single row antenna array with the opening slot below is set as vertical polarization, as shown in Figure 4. The model of cross installation of two single row horizontal and vertical polarization arrays is shown in Figures 3 and 4. This design only requires processing 22 rows of antenna array to complete array assembly (11 rows of horizontal and vertical polarization), thereby saving the processing cost of the entire array.

In addition, the optimized Vivaldi antenna has a conical open end with width of 27 mm, a coupling slot line with width of 1.22 mm, and a circular resonant cavity with radius of 7.5248 mm to improve the gain and pattern of the antenna. The length of the fan-shaped microstrip line is 9.5077 mm to enhance the matching between the antenna and the port. Several through holes with a radius of 0.25 mm are also designed at the edge of

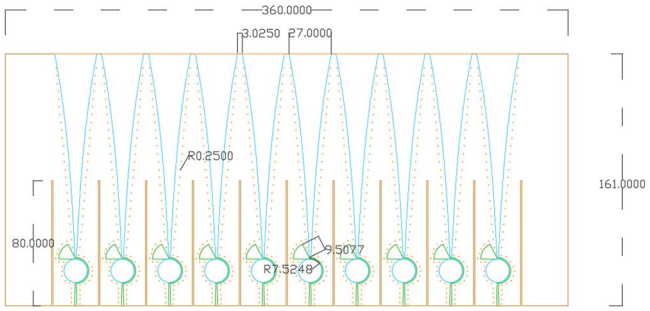

Figure 5. Single row array of vertical polarization and its parameter labeling.

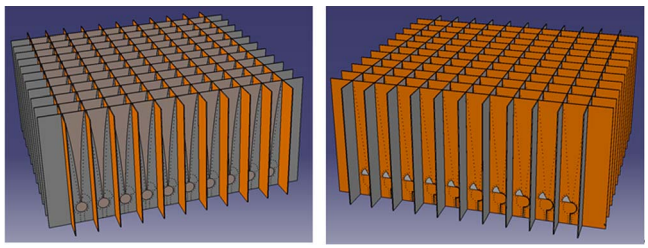

Figure 6. Front and rear model diagrams of the assembled array.

the antenna radiation end to improve the surface current of the array element. The height of the cross installation slot for a single row antenna is set to 80 mm, with a width of 0.85 mm. The entire single row PCB has a width of 360 mm, including 10 array elements and outer edges, as shown in Figure 5.

The antenna array model after integrated assembly is shown in Figure 6. The overall size of the array is 360 mm × 360 mm. When the array is placed at the focal field position of the reflector, the area covered by the array is 300.25 mm × 300.25 mm.

2.3. Design of Beam

Due to the design difficulty of array being the 0.7–1.8 GHz bandwidth to be achieved, combined with the limitation of the number of elements in 100 mag, the final array size in the tightly coupled design is only 300 mm × 300 mm. This is different from the sequence of array design based on field of view of the telescope (Ma et al. 2021). However, for situations where the testing conditions for reflector are not currently available, this design scheme meets the performance of an independent array and can be measured and verified in microwave technology laboratory of the XAO. Therefore, beam design will also be based on this array model.

First, place this fixed size PAF array in the focal field at different parallel wave incidence angles to verify the range of focal field that the array can cover. Figure 7 shows the normalized −3 dB edge taper area and array coverage of the focal field when parallel waves incident axially as well as the off-axis of one and two beams on the reflector at 0.7 GHz. The

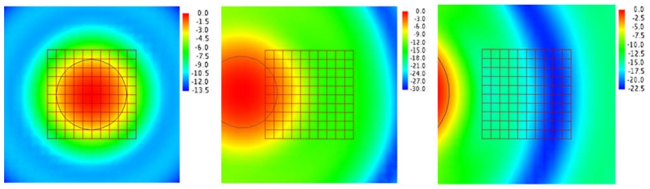

Figure 7. Focal field and array coverage of axial and off-axis one and two beams at 0.7 GHz.

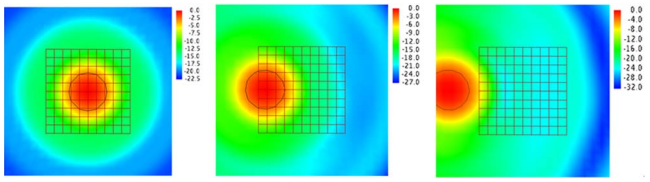

Figure 8. Focal field and array coverage of axial and off-axis one and two beams at 1.25 GHz.

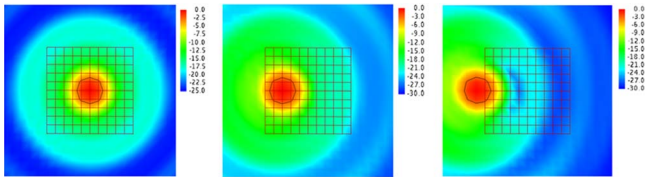

Figure 9. Focal field and array coverage of axial and off-axis one and two beams at 1.8 GHz.

array is the grid area in the figure, and the horizontal and vertical lines represent the horizontal and vertical polarized antenna arrays, respectively. It can be seen that the array can fully cover the −3 dB edge taper area of the axial beam at 0.7 GHz; When the incident wave is off-axis by one beamwidth, the array can only cover a small portion of the −3 dB edge taper area; When the incident wave is off-axis by two beamwidths, the array is no longer able to cover the area.

Figure 8 shows the situation at 1.25 GHz. When the incident wave is off-axis by one beamwidth, the array can cover most of the −3 dB edge taper area.

Figure 9 shows the situation at 1.8 GHz. When the incident wave is off-axis by two beamwidths, the array can only cover a small portion of the −3 dB edge taper area.

Combined with the above analysis of the focal field, our design only uses array elements within the −3 dB edge taper area to forming a single beam. The relationship between the array and the corresponding beams at the three frequency points is shown in Figure 10. The circular area shown by the black line represents the −3 dB edge taper area of the corresponding frequency, and the red grid represents the array of corresponding sizes. From the figure, it can be seen that the Vivaldi antenna array can only forming one beam at 0.7 GHz,

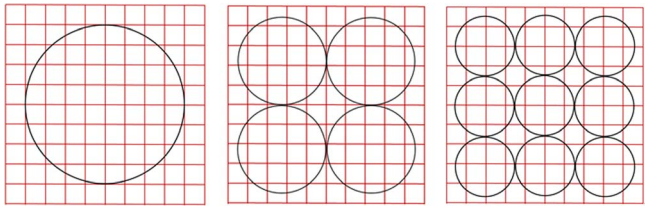

Figure 10. Layout diagram of beams formed instantaneously at three frequency points.

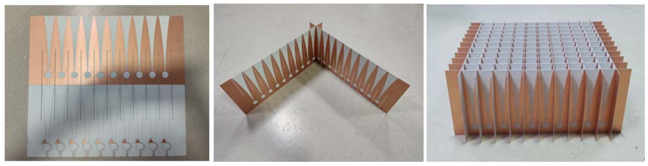

Figure 11. Single row horizontal and vertical polarized antennas and cross assembled array.

four continuous beams at 1.25 GHz, and nine continuous beams at 1.8 GHz.

3. Development and Measurement of PAF Array Prototype

3.1. Development of Array

3.1.1. Fabrication of Array

The Vivaldi antenna array adopts PCB form, and the dielectric substrate is Rogers4003c (with a dielectric constant of 3.38). It is formed by connecting and arranging 10 Vivaldi antenna units in a single row, with the horizontal polarization antenna installation slot opening on the upper side and the vertical polarization on the lower side, as shown in Figure 11. The single row horizontal and vertical polarized antennas are cross assembled through upper and lower installation slots, as shown in Figure 11. The two polarizations each consist of 11 Vivaldi antenna rows, which are ultimately assembled into a single antenna array through cross assembly, as shown in Figure 11.

3.1.2. Assembly of Array

The next step is to design the array base plate fixing and installation components. In addition to fixing the entire Vivaldi antenna array, the assembly of the antenna array should also consider the welding of 110 × 2 SMA connectors. First, a base plate is designed at the bottom of the array, with a model shown in Figure 12. One hundred through-holes are designed to install a pair of adjacent SMA connectors for horizontal and vertical polarized Vivaldi antennas. At the same time, it is convenient for the welding gun to penetrate the inner side of

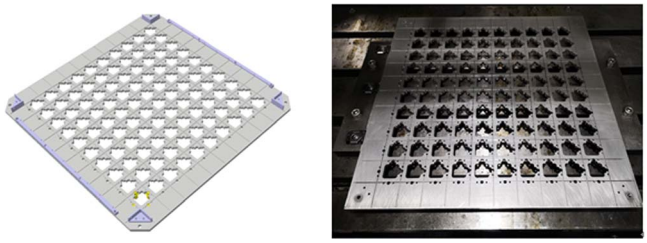

Figure 12. Model and prototype of base plate.

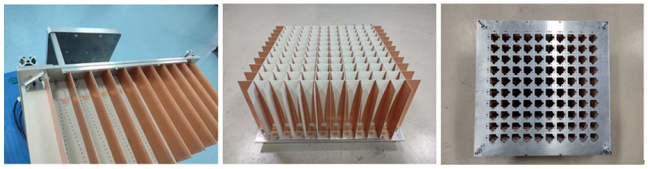

Figure 13. Fixing clips and top and bottom pictures of the array after assembly.

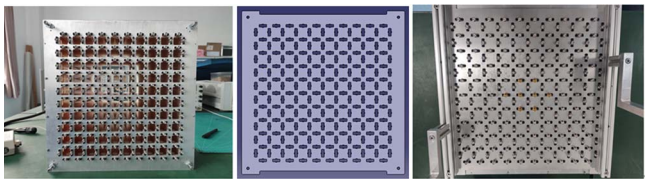

Figure 14. Pictures of SMA welded array, back plate model and after installation.

the through-hole to weld the antenna feeding port and SMA pins. A groove is set at the contact position with the antenna array on the upper part of the base plate, with a depth of 2 mm. Long strip shaped fixing clips are designed on both sides of the vertical polarization direction of the base plate (light blue long strip component in Figure 12) to fix the nine rows of antennas with the opening slot below. At the same time, right angle shaped fixing clips are designed at the four corners of the base plate (light blue right angle component in Figure 12) to fix the edges of array for two mutually perpendicular rows of antennas. The final processed base plate is shown in Figures 12.

Figure 13 shows the top and bottom pictures of the array after the installation of the long strip fixed clips and base plate. It can be seen that the base plate can firmly fix the antenna array in the designated position, and at this time, SMA connectors have not been installed at each through-hole of the base plate.

After installing the base plate, we installed 220 SMA connectors and welded them accordingly, as shown in Figure 14. In order not to affect the performance of the array, a back plate was designed at the bottom of the array to block the installation through holes, as shown in Figure 14. This back plate is equipped with 220 through holes to ensure the normal connection of SMA connectors is not affected. Finally, the bottom photo of the entire antenna array after assembly is shown in Figure 14.

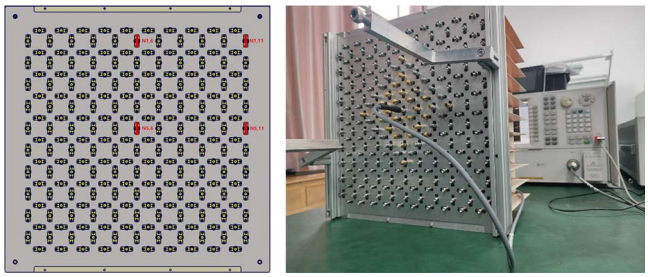

Figure 15. Position of four elements and laboratory testing of return loss.

3.2. Measurement of Array

3.2.1. Return Loss

Due to the temporary lack of testing components for the active array, we only tested the return loss of each element of the passive array. Considering the large number of array elements, we have selected four typical positions of element in the vertical polarization (N1,6, N1,11, N5,6, N5,11). Figure 15 shows the corresponding positions of four typical array elements in the array back plate, and Figure 15 shows testing picture of N5,6 for return loss using a vector network analyzer.

Figure 16 shows the results of passive return loss for the four elements mentioned above. From the results, it can be seen that the S11 of each element remains below −10 dB at 1.25 GHz, but the −10 dB impedance bandwidth of each array element cannot cover the designed bandwidth of 0.7–1.8 GHz. Because all ports of the entire array are excited in the simulation, and the active array elements exhibit broadband characteristics due to strong coupling effects, especially for the element located at the center of the array, as shown in Figure 3. During actual measurement with experimental conditions, the tested array is a passive array, all ports are in a non excited state, thus unable to exhibit broadband performance under strong coupling. However, the measured passive return loss of the four elements can still show the trend of the active array by adding several matching loads to the ports around the test element, such as the −10 dB impedance bandwidth of the element N5,6 located at the center of the array, which is significantly better than the other elements, especially in the mid to high frequency it has been basically achieved below −10 dB.

3.2.2. Pattern of Element

Next, we test the patterns of each independent element of the passive array. A pattern testing platform is built in the laboratory, with the signal source of Agilent E8257D (250 KHz–67 GHz), and the transmitting antenna is a double ridge standard gain horn of HD-0660DRHA10N (0.6–6 GHz).

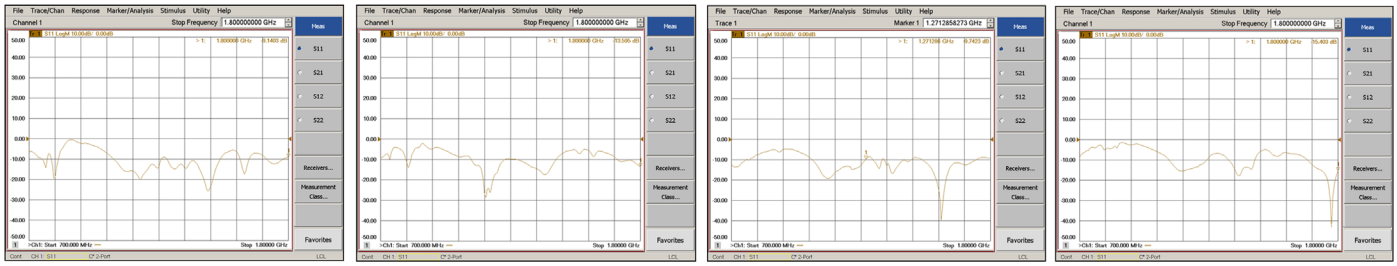

Figure 16. Test results of passive return loss for four vertically polarized elements.

Figure 17. Laboratory testing of pattern.

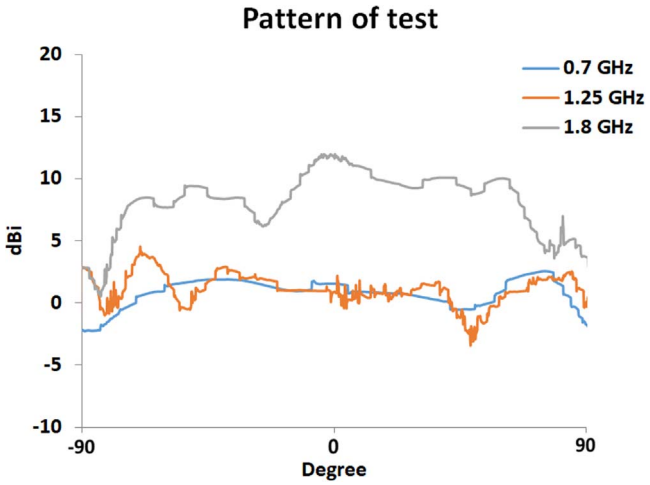

Figure 18. Test results of pattern for central element (N5,6) at 0.7, 1.25 and 1.8 GHz.

The power acquisition selected from Agilent U2004A power probe (9 KHz–6 GHz). As shown in Figure 17, the transmitting antenna on the left is vertically polarized, 3.2 m away from the tested antenna array on the right, and the power probe is connected to the port of vertically polarized tested element.

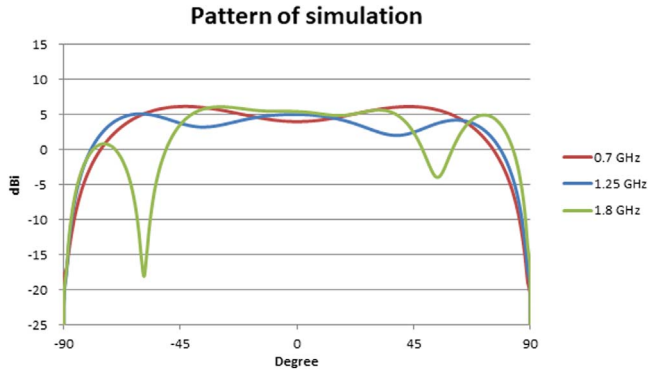

Figure 19. Simulation results of pattern for central element (N5,6) at 0.7, 1.25 and 1.8 GHz.

During testing, the array antenna is controlled to horizontally scan the transmitting antenna end, while data are collected by the power probe.

Figure 18 shows the pattern of the vertically polarized central array element N5,6 at 0.7, 1.25, and 1.8 GHz. During the testing, the pattern testing platform set the signal source transmission power to 5 dBm, the transmission antenna gain was 10.58 dB, the cable and connector losses were 12 dB, and the theoretical attenuation in free space at a testing distance of 3.2 m was 39.5, 44.5 and 47.7 dB (Wang & Xue 2013). Finally, the measured gains were calculated to be 2.62, 4.52, and 12.02 dBi.

Figure 19 shows the simulation results of vertical polarized central element N5,6, with simulated gains of 6.18, 5.12 and 6.12 dBi, respectively. Through comparison, it can be seen that there is a certain difference between the measured gain and the simulation results, especially in test result of 1.25 GHz, there is a significant collapse at the center of the pattern contour, making the sidelobe gain on both sides of the pattern significantly higher than the center.

In order to comprehensively understand the actual situation of each element and find the cause of the center collapse of the pattern at 1.25 GHz, combined with the symmetry of the entire array, we selected six elements from N5,1 to N5,6 in the horizontal direction and five elements from N1,6 to N5,6 in the

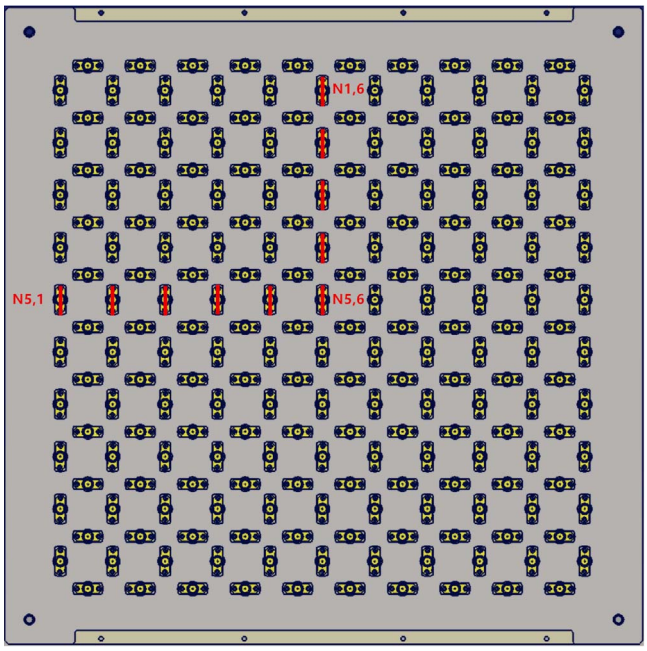

Figure 20. Positions of the measured elements in the horizontal and vertical directions.

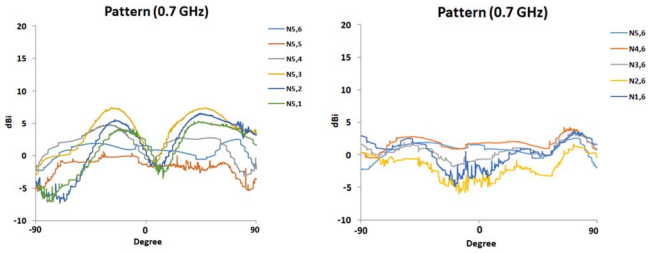

Figure 21. Test results of pattern for element in the horizontal and vertical direction at 0.7 GHz.

vertical direction for testing and comparison. The corresponding array positions of each tested element are shown in Figure 20.

Figure 21 shows the measured results of the vertical polarized elements by selected at 0.7 GHz. Figure 22 shows the pattern simulation results of N5,6, N5,1, and N1,6 at 0.7 GHz. It can be seen that in the horizontal direction, as the measured element moves from the center to the left edge, the measured gain increases, and the contour of the pattern gradually shows a bimodal shift to the right. The measured gain of N5,1 is 5.32 dBi (simulation is 6.26 dBi). In the vertical direction, as the measured array element moves from the center to the upper edge, the measured gain slightly decreases, and the pattern contour does not change significantly. The measured gain of N1,6 is 3.82 dBi (simulated as 5.76 dBi).

Figures 23 and 24 show the measured and simulated results of the pattern at 1.25 GHz. It can be seen that in the horizontal direction, the measured gain of the element is slightly

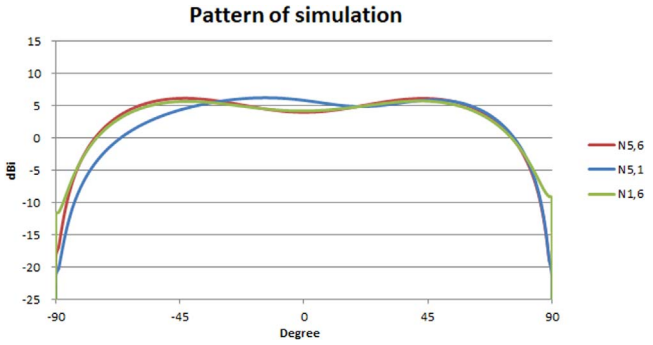

Figure 22. Simulation results of pattern for N5,6, N5,1 and N1,6 at 0.7 GHz.

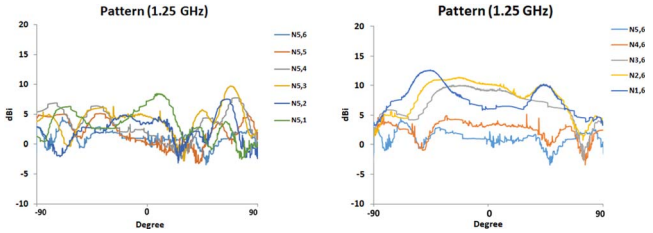

Figure 23. Test results of pattern for element in the horizontal and vertical direction at 1.25 GHz.

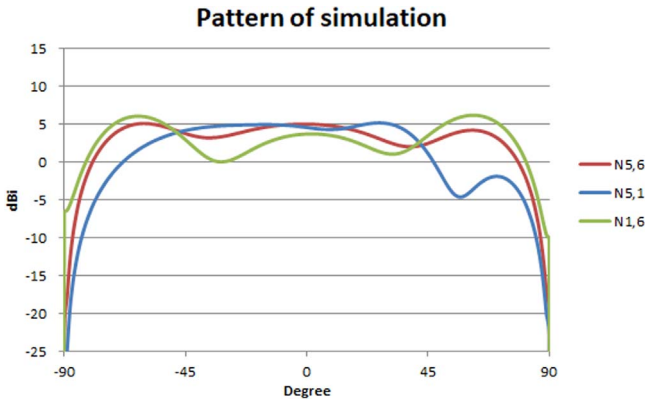

Figure 24. Simulation results of pattern for N5,6, N5,1, and N1,6 at 1.25 GHz.

enhanced, and the central contour of the pattern gradually protrudes and slightly shifts to the right side. The measured gain of N5,1 is 8.52 dBi (simulation is 5.21 dBi). In the vertical direction, the measured gain of the element is significantly enhanced, and the main lobe contour of the pattern is becoming more obvious. The measured gain of N1,6 is 12.62 dBi (simulated as 6.21 dBi).

Figures 25 and 26 show the measured and simulated results of the pattern at 1.8 GHz. It can be seen that in the horizontal direction, the measured gain change of the element is not significant, and the main lobe of the pattern central slightly shifts to the right side. The measured gain of N5,1 is 11.62 dBi

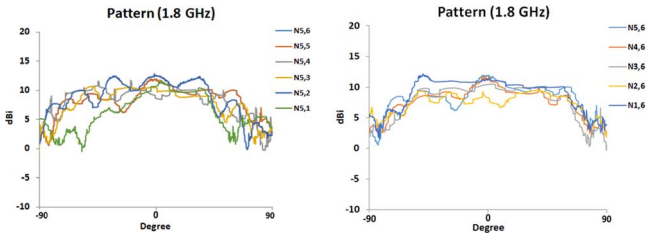

Figure 25. Test results of pattern for element in the horizontal and vertical direction at 1.8 GHz.

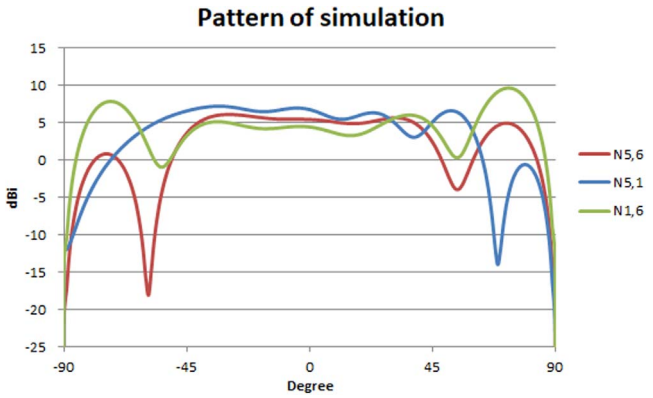

Figure 26. Simulation results of pattern for N5,6, N5,1 and N1,6 at 1.8 GHz.

(simulation is 7.23 dBi). In the vertical direction, the measured gain change of the element is also not significant, and the central contour of the pattern gradually flattens out. The measured gain of N1,6 is 12.22 dBi (simulated as 9.68 dBi).

3.2.3. Beamforming

After completing the independent element testing, we combined with the existing 32-channel power divider with the highest number of channels (QPD32-700-2700-30-S, 32-channel power divider produced by Qualwave Inc., 0.7–2.7 GHz), and selected 32, 18, and eight elements to form one beam at 0.7, 1.25 and 1.8 GHz, as shown in Figure 27. The red mark represents the positions of the element corresponding to the axial beam of the forming three frequency points, and the yellow line represents the −3 dB edge taper area of the focal field.

Due to the lack of a reflector antenna in the laboratory, it is not possible to place the array at the focal plane for actual measurement, as in the practical application of PAF receiver. Therefore, we conducted analog beamforming testing and validation of the independent array using laboratory conditions. The beamforming adopts a uniform excitation method of equal amplitude and phase. 32, 18, and eight vertically polarized elements were selected at 0.7, 1.25, and 1.8 GHz. The output

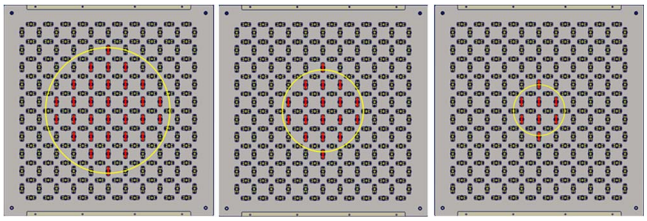

Figure 27. Positions of the elements required for forming axial beam at 0.7, 1.25 and 1.8 GHz.

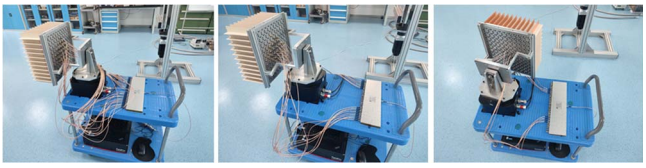

Figure 28. Analog beamforming network under uniform excitation at 0.7, 1.25 and 1.8 GHz.

ports of each element were connected a 1.5 m cable to 32-channel power divider. After the power divider synthesizes, it is then transmitted to the power probe by a 1.5 m cable for collection. Figure 28 shows the analog beamforming network under uniform excitation at 0.7, 1.25, and 1.8 GHz.

Continuing to use the various parameters set of independent element testing, the difference is that the cable and connector losses are 20 dB. The pattern of independent array under equal amplitude and phase excitation at 0.7, 1.25, and 1.8 GHz is shown in Figure 29. Finally, the measured gains were calculated to be 19.32, 13.72, and 15.22 dBi.

Figure 30 shows the simulation results of the forming pattern under uniform excitation, with gains of 6.64, 7.49, and 8.14 dBi. Based on the measured results, it can be seen that with the increase of the number of elements participating in the forming beam, the measured gain of the forming beam has been significantly improved, and the beamwidth also decreases with the increase of frequency. However, the measured result of the 1.25 GHz forming pattern are similar to the center independent N5,6, with a clear collapse in the pattern contour at the center position.

3.2.4. Beam Scanning

As mentioned in Section 2.3, the existing array can achieve the function of scanning one beamwidth at 1.8 GHz. Referring to Figure 9, there is no significant change in the focal field −3 dB edge taper area under the axial beam and off-axis one beam at 1.8 GHz. Therefore, it can be concluded that the number of array elements required to form any beam at the same frequency throughout the array range is consistent.

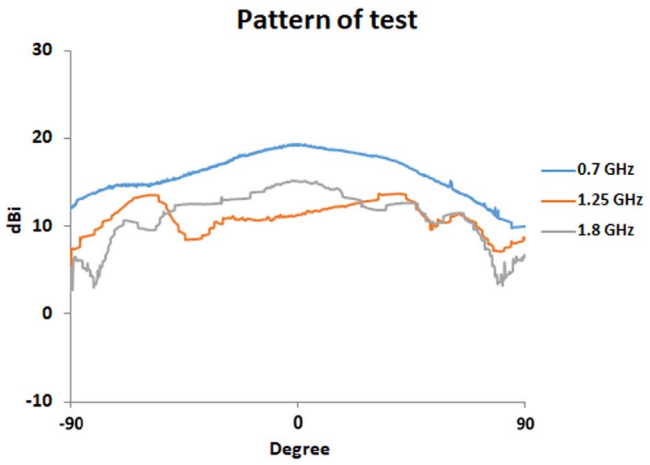

Figure 29. Test results of forming pattern for independent array at 0.7, 1.25 and 1.8 GHz.

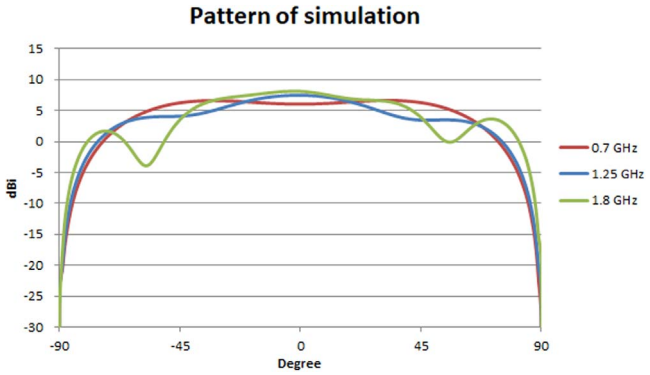

Figure 30. Simulation results of forming pattern for independent array at 0.7, 1.25 and 1.8 GHz.

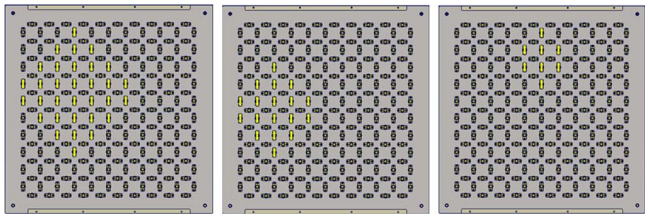

Figure 31. Positions for edge beam scanning in the *D*, *X* and *Y*-axis at 0.7, 1.25 and 1.8 GHz.

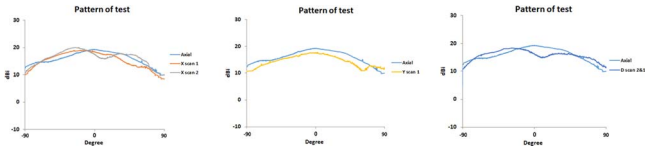

Figure 32. Test results of pattern for each scanning beam of the array at 0.7 GHz.

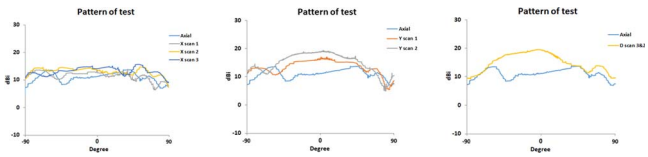

Figure 33. Test results of pattern for each scanning beam of the array at 1.25 GHz.

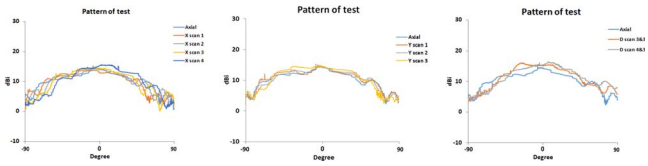

Figure 34. Test results of pattern for each scanning beam of the array at 1.8 GHz.

Considering that when PAF performs beam scanning, beams with different scanning angles are formed using the elements within the corresponding focal field position at different incident angles as described in Section 2.3. At the same time, considering the arrangement of the array, the forming beams can be scanned by row, by column, or by row and column simultaneously based on the array. The yellow mark in Figure 31 represents the 32 elements corresponding to forming edge beam during *D*-axis scanning at 0.7 GHz, the 18 elements during *X*-axis scanning at 1.25 GHz, and the eight elements during *Y*-axis scanning at 1.8 GHz.

Figure 32 shows the pattern measured results of the vertical polarization center axial beam and the *X*, *Y*, and *D*-axis scanning beams at 0.7 GHz (uniformly excited). In the horizontal direction, as the 32 elements set move from the center to the left edge, the measured gains of the scanning beams that shift two columns are 19.02 and 20.12 dBi. In the vertical direction, as the 32 elements set move from the center to the upper edge, the measured gain is 17.82 dBi. In the diagonal direction, as the 32 elements set move from the center to the upper left edge, the measured gain is 18.42 dBi.

Figure 33 shows the measured results of pattern at 1.25 GHz. In the horizontal direction, as the 18 elements set move from the center to the left edge, the measured gains of the scanning beams that shift three columns are 13.92, 14.72, and 15.62 dBi. In the vertical direction, as the 18 elements set move from the center to the upper edge, the measured gains are 17.02 and 19.42 dBi. In the diagonal direction, as the 18 elements set move from the center to the upper left edge, the measured gain is 19.62 dBi.

Figure 34 shows the measured results of the pattern at 1.8 GHz. In the horizontal direction, as the eight elements set move from the center to the left edge, the measured gains are 13.82, 14.32, 14.72, and 15.72 dBi. In the vertical direction, as

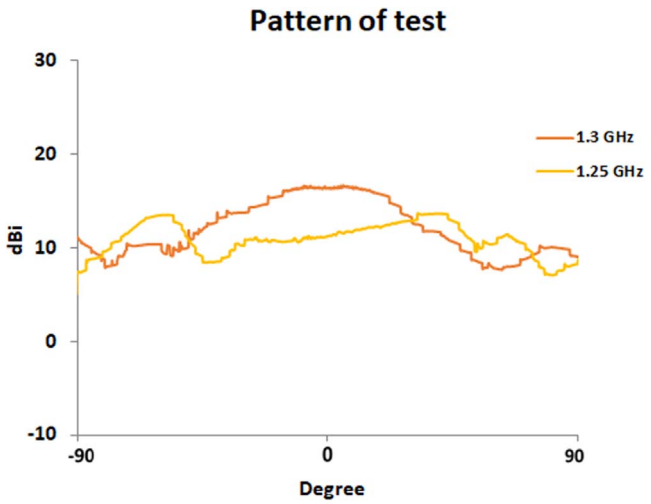

Figure 35. Test results of pattern for axial beam of 18 elements at 1.25 and 1.3 GHz.

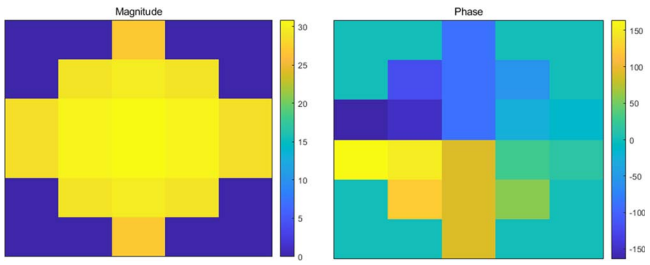

Figure 36. Weights of the conjugate matching method for 18 elements at 1.25 GHz.

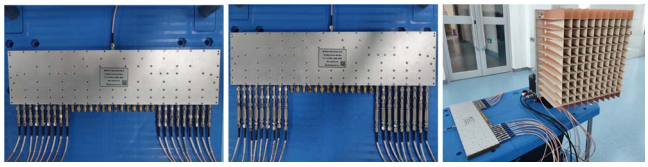

Figure 37. Analog beamforming network for conjugate field matching and its testing.

the eight elements set move from the center to the upper edge, the measured gains are 15.12, 14.52, and 14.82 dBi. In the diagonal direction, as the eight elements set move from the center to the upper left edge, the measured gains are 16.12 and 16.52 dBi.

4. Discuss

Based on the measured patterns of the independent element and array mentioned above, the results show that the patterns of central element and axis beam of the array have obvious defects at 1.25 GHz, as shown in Figures 18 and 29. Further analysis and discussion are necessary.

In Figure 23, as the measured array element moves from the center to the left edge, the test gain slightly increases, which is similar to the simulation results. However, as the measured element moves from the center to the upper edge, the test gain shows a significant increase, which is completely opposite to the simulation results and trends.

Due to the fact that the current array design has fixed, the characteristics of the array elements cannot be changed, and the PAF receiver will adjust the actual pattern using a beamformer, we selected 18 elements that form the axial beam at 1.25 GHz to test pattern when uniformly excited at 1.3 GHz of adjacent frequency. The test results are shown in Figure 35. It can be seen that when the transmission signal changes to 1.3 GHz, the contour of the pattern of the tested array has significantly improved. The position where the collapse occurred at 1.25 GHz has a significant uplift at 1.3 GHz, and the center position presents a good Gaussian distribution contour.

Considering that 1.25 GHz is the central frequency of the entire bandwidth and the performance of this frequency is of particular concern, we consider adopting an appropriate weighting method to improve the current concave pattern. The weighting method of equal amplitude and phase excitation previously adopted was only for the convenience of implementation, but in practical applications, PAF receivers generally apply different excitation based on requirements. The conjugate matching method is a relatively basic method in the beamforming algorithm of PAF receiver. We use the simulation results of the 1.25 GHz focal field to re weight the 18 elements, and the magnitude and phase excitations corresponding to each array element required to synthesize the central axial beam are shown in Figure 36.

The analog beamforming network with only amplitude and amplitude-phase adjustment weighted by conjugate field matching are shown in Figure 37. It can be seen that the attenuators and phase shifters are involved in the amplitude and phase adjustment of 18 elements.

Figure 38 shows the measured pattern of the central axial beam of an independent array under conjugate matching excitation with only amplitude and amplitude-phase adjustment at 1.25 GHz. It can be seen that compared with the pattern with uniform excitation, the gain has increased from 13.72 to 14.17 and 13.97 dBi, the sidelobe level has decreased from −0.21 to −2.74 and −3.08 dB, and the main beam direction has also been adjusted back from 33° to 17° and −13°. It can be seen that the conjugate matching excitation effectively improves the sidelobe level and main beam direction of the pattern at 1.25 GHz. We believe that if a more flexible digital beamforming method and maximum signal-to-noise ratio beamforming algorithm are adopted, the testing performance can be further optimized, which is also our next work.

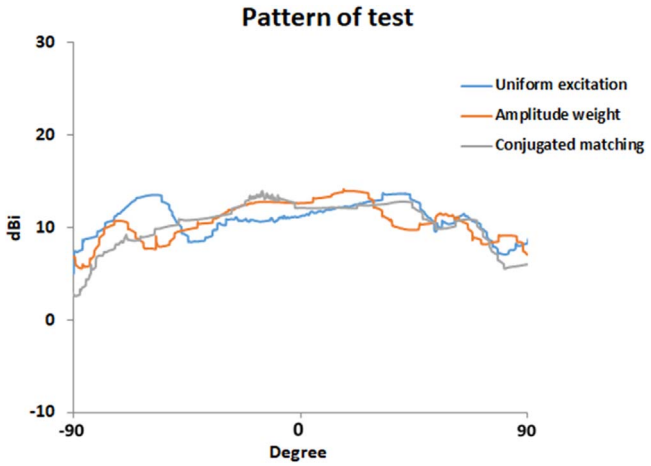

Figure 38. Test results of pattern for uniform excitation and conjugate matching at 1.25 GHz.

5. Conclusion

This article combines the requirements of a phased array receiver in the 20 cm band of the QiTai 110 m telescope of XAO and develops a front-end array of broadband PAF receiver operating at 0.7–1.8 GHz. This array is a PCB structure Vivaldi antenna array with dual line polarized, each polarized antenna arranged according to 11×10 in a rectangular, the size of the array is 360 mm $\times$ 360 mm. The design uses 32, 18 and eight elements in -3 dB edge taper area of the focal field to form one beam at 0.7, 1.25 and 1.8 GHz. Due to the temporary lack of related microwave components, this article conducted passive S-parameter and pattern performance tests on the array based on the conditions of the Microwave Technology Laboratory of XAO. The test results indicate that the return loss of the array center element is -12.5 dB@1.25 GHz, and the measured axial beam gains of the array under uniform excitation of the analog beamforming network are 19.32 dBi@0.7 GHz, 13.72 dBi@1.25 GHz and 15.22 dBi@1.8 GHz. Combining the beam scanning method of the PAF receiver in the reflector, the pattern measurement of the different position array element sets required for PAF beam scanning are carried out under independent array conditions. At the same time, considering the issue of concave contour of the 1.25 GHz central axial beam pattern under uniform excitation, the conjugate matching excitation method is used to conduct forming pattern testing at 1.25 GHz. After optimization, the gain was increased to 13.97 dBi, the sidelobe level decreased to -3.08 dB, and the main beam direction was adjusted back to $-13°$. Although there are certain differences between the above test and simulation results, which are related to the conditions of the array testing platform and the laboratory testing environment, the performance verification of the passive array carried out in this article provides experience for future system composition more complex active array. The implementation of related work has also enabled team members to further master the phased array receiver and its front-end feed array technology, which has good guiding significance for future performance verification after the array is installed on the reflector. Next, the project team needs to establish a complete phased array receiver, combined with a more comprehensive maximum signal-to-noise ratio beamforming algorithm and digital beamforming network to carry out related work, in order to better assist in the development of future 20 cm band PAF receiver.

Acknowledgments

This work was supported by the National Key R&D Program of China (No. 2022YFC2205303), the National Natural Science Foundation of China (11973078), the Chinese Academy of Sciences (CAS) "Light of West China" Program (2020-XBQNXZ-018), the Natural Science Foundation of Xinjiang Uygur Autonomous Region (2022D01A358, 2022D01A157) and the Research on the science and technology partnership program and international science and technology cooperation program of Shanghai Cooperation Organization (2020E01041). The work was partly supported by the Operation, Maintenance and Upgrading Fund for Astronomical Telescopes and Facility Instruments, budgeted from the Ministry of Finance of China (MOF) and administrated by Chinese Academy of Sciences.

References

Chippendale, A. P., Beresford, R. J., Deng, X., et al. 2016, in Int. Conf. Electromagnet. Adv. Appl. (Cairns: IEEE), 909
Cortes-Medellin, G., Vishwas, A., Parshley, S. C., et al. 2015, ITAP, 63, 2471
Deng, X. P., Chippendale, A. P., Barr, E., et al. 2017, Proc. Int. Astron. Union, 13, 330
Dunning, A. 2022, International Phased Array Feed & Advanced Receiver Workshop, Sydney, 2022, 1–23, https://research.csiro.au/ratechnologies/wp-content/uploads/sites/295/2022/11/PAFAR2022-Dunning-CryoPAF_for_Parkes.pdf
Hay, S. G., O'Sullivan, J. D., Kot, J. S., et al. 2007, in 2nd Eur. Conf. Antennas and Propagation (Edinburgh: IEEE), 1–5
He, C. Y., & Li, B. 2013, Annual Journal of the Shanghai Astronomical Observatory, CAS, 00, 53
Ma, J., Pei, X., Wang, N., et al. 2019, SCPMA, 49, 6
Ma, J., Wu, Y., Xiao, S., et al. 2021, RAA, 21, 90
Navarrini, A., Monari, J., Scalambra, A., et al. 2018, in 2018 II URSI Atlantic Radio Science Meeting (Gran Canaria: IEEE), 1–4
Roshi, D. A., Shillue, W., Simon, B., et al. 2018, AJ, 155, 202
Tian, J. Y. 2023, Master Dissertation for Electronic Science Research Institute of CETC, 2023, 15
Tian, J. Y., Du, B., Wu, Y., et al. 2022, Chinese Journal of Radio Science, 37, 58
Wang, J. Z., & Xue, Z. H. 2013, Posts and Telecommunications Press, 1, 103
Wang, N. 2014, SCPMA, 44, 783
Wang, N., Xu, Q., Ma, J., et al. 2023, SCPMA, 66, 154
Wu, Y. 2013, Doctoral Dissertation, Univ. of Xidian, 20131
Wu, Y., Du, B., Jin, C. J., et al. 2013, Chinese Journal of Radio Science, 28, 348
Zhang, Y., & Brown, A. K. 2011, ITAP, 59, 3927